

RESEARCH ARTICLE | JANUARY 19 2022

Hybrid gyrokinetic ion/fluid electron simulation of toroidal tearing modes **FREE**

Ruibo Zhang ; Yang Chen  ; Lei Ye ; Nong Xiang



Physics of Plasmas 29, 012108 (2022)

<https://doi.org/10.1063/5.0067813>

 CHORUS



View
Online



Export
Citation

CrossMark

Articles You May Be Interested In

Finite Larmor radius effects on the ($m = 2$, $n = 1$) cylindrical tearing mode

Physics of Plasmas (April 2015)

Gyrokinetic analysis of tearing instabilities in a collisionless plasma

Physics of Plasmas (March 2011)

Gyrokinetic simulations of the tearing instability

Physics of Plasmas (November 2011)

Hybrid gyrokinetic ion/fluid electron simulation of toroidal tearing modes

Cite as: Phys. Plasmas **29**, 012108 (2022); doi: [10.1063/5.0067813](https://doi.org/10.1063/5.0067813)

Submitted: 19 August 2021 · Accepted: 29 December 2021 ·

Published Online: 19 January 2022



View Online



Export Citation



CrossMark

Ruibo Zhang,^{1,2} Yang Chen,^{3,a)} Lei Ye,^{1,b)} and Nong Xiang¹

AFFILIATIONS

¹Hefei Institutes of Physical Science, Chinese Academy of Sciences, Hefei 230031, China

²University of Science and Technology of China, Hefei 230026, China

³Center for Integrated Plasma Studies, University of Colorado at Boulder, Boulder, Colorado 80309, USA

^{a)}Author to whom correspondence should be addressed: yang.chen@colorado.edu

^{b)}Electronic mail: lye@ipp.ac.cn

ABSTRACT

The effects of toroidicity and kinetic ions on the resistive tearing mode are systematically studied with the gyrokinetic particle-in-cell simulation code GEM [Y. Chen and S. E. Parker, J. Comput. Phys. **220**, 839 (2007)] and compared with analytic theory. A new field solver in toroidal geometry has been developed for the simulation of low- n ($n = 1, 2$) modes in tokamaks. It is found that the toroidal effect significantly reduces the growth rate of the tearing mode. The toroidal effect can also increase the radial width of the tearing mode and change the scaling between the radial mode width and resistivity due to the toroidal pressure term in the electron continuity equation. The kinetic effects of ions can decrease the growth rate of the tearing mode. The plasma flux-surface shaping is found to have significant effect on the tearing mode.

Published under an exclusive license by AIP Publishing. <https://doi.org/10.1063/5.0067813>

I. INTRODUCTION

The tearing mode has been acknowledged as one of the most dangerous products of magnetic reconnection^{1–3} in today's fusion devices. The magnetic energy can transform into kinetic energy, thermal energy, and radiant energy during the process of magnetic field lines breaking and reconnecting near the current sheets. It is also a crucial instability which may cause the sawtooth oscillations and even lead to major disruptions in tokamaks.⁴ Due to the great importance of the tearing mode in fusion plasma, numerous theoretical works^{5–9} have been carried out to study the linear and nonlinear properties of the tearing mode.

The toroidal effect is important in realistic tokamaks due to the non-uniformity of the magnetic field and the coupling of the poloidal modes. For a tokamak with a small aspect ratio, the toroidal coupling effect could be very strong, and the peak amplitude of the resonant harmonic could even exceed that of the vacuum field.¹⁰ It has been pointed out that the toroidal effect could lead to a reduction in the growth rates of the tearing mode.^{11,12} Besides, some mechanisms can only be considered in toroidal geometry, such as the magnetic drift (v_D) effect of ions.

The tearing mode is essentially a multi-scale phenomenon, and it is difficult to predict its behavior analytically. Specifically, the timescale

of the tearing mode ranges from the Alfvén time to the collisional dissipation time, and the spatial scale ranges from the electron skin depth to the device size. Due to these properties, the kinetic effects of ions near the tearing layer can be important. Much effort has been made to study the kinetic effects on the tearing mode in the past few decades. The kinetic theory for the classic tearing mode was developed in cylindrical geometry by Hazeltine *et al.*¹³ Drake and Lee first predicted that the growth rate of the tearing mode with the kinetic effect scales as $\gamma \sim \nu_c^{1/3}$ in the semi-collisional regime and $\gamma \sim \nu_c^{3/5}$ in the collisional regime, ν_c being the collision frequency.¹⁴ Moreover, kinetic effects of energetic particles can affect the tearing mode's behavior prominently in high temperature tokamak devices.¹⁵ Nevertheless, the study of the tearing mode with fully kinetic effects is still challenging for both analytic theory and numerical simulation due to the multiple scale property of the tearing mode.^{16–19}

Gyrokinetic theory and simulation are a powerful tool to study kinetic effects on tearing modes.^{16,20–22} However, due to the physical complexity mentioned above and the numerical difficulties, it is still a great challenge to simulate the low- n tearing mode using gyrokinetic simulation. The evolution of the small scale collisionless tearing mode in a sheared slab geometry was first studied with nonlinear gyrokinetic simulations by Sydora.²⁰ An improved gyrokinetic electron/fully

kinetic ion (GeFi) particle simulation scheme was developed for studying the linear collisionless tearing mode in a two-dimensional Harris current sheet with a realistic ion-to-electron mass ratio.²³ Previous simulations with the gyrokinetic toroidal code (GTC) found that the ion kinetic effects can partially stabilize the cylindrical tearing mode by reducing the radial mode width.¹² Linear gyrokinetic simulations by the global continuum turbulence code GWK concluded that finite Larmor radius (FLR) effects can give rise to a finite rotation frequency of the tearing mode.¹⁹

GEM is a gyrokinetic δf Particle-in-Cell (PIC) code which was first developed to study drift wave turbulence including kinetic electrons and electromagnetic effects.²⁴ A fluid electron model was later developed to more efficiently simulate MHD waves.²⁵ However, it is still beyond the capability of GEM to simulate low- n modes in toroidal geometry with poloidal mode coupling effects. This is because a high- n approximation, previously used in the field solvers, is not valid for low- n ($n = 1, 2$) modes. A low- n field solver has recently been developed in cylindrical geometry and applied to study the ($m = 2, n = 1$) cylindrical tearing mode,²⁶ but it does not include the effect of poloidal coupling and therefore is not applicable to toroidal low- n modes.

In this work, we develop a new low- n field solver in the magnetic flux coordinates for the GEM code. With this new field solver, the $n = 1$ tearing modes in toroidal geometry are systematically studied. The effects of toroidicity, gyrokinetic ions, and plasma shape on the resistive tearing mode are studied. The remaining part of this paper is organized as follows. The basic equations of the hybrid gyrokinetic ion/fluid electron model and the algorithm of the new field solver are described in Sec. II. The effects of toroidicity, gyrokinetic ions, and plasma shape on the resistive tearing mode are studied in Sec. III. Conclusion is drawn in Sec. IV.

II. BASIC EQUATIONS AND LOW- n FIELD SOLVER

In this work, we consider a general axisymmetric toroidal equilibrium magnetic field $\mathbf{B} = \frac{f(\psi)}{R} \hat{\zeta} + \nabla \zeta \times \nabla \psi(r)$ in toroidal coordinates (r, θ, ζ), where r, θ , and ζ indicate radial, poloidal, and toroidal directions, respectively. $\psi(r)$ indicates the poloidal flux function, and $f(\psi)$ indicates the arbitrary flux function.

The equilibrium flux-surface shape is specified by the Miller model,²⁷

$$\begin{cases} R = R_0(r) + r \cos [\theta + (\sin^{-1} \delta(r)) \sin \theta], \\ Z = \kappa(r) r \sin \theta, \end{cases} \quad (1)$$

with $R'_0 = \frac{dR_0}{dr}$ the Shafranov shift, $\kappa(r) = \kappa_0$ the elongation, and $\delta(r) = \delta_0 (r/a)^2$ the triangularity, where R_0 is the major radius at the magnetic axis and a is the minor radius.

GEM uses the field-aligned coordinates defined by

$$\begin{cases} x = r - r_0, \\ y = \frac{r_0}{q_0} \left(\int_0^\theta \hat{q}(r, \theta') d\theta' - \zeta \right) = \frac{r_0}{q_0} (q\theta_f - \zeta), \\ z = q_0 R_0 \theta, \end{cases} \quad (2)$$

here, r_0 is a reference radius, $\theta_f = \frac{1}{q} \int_0^\theta \hat{q}(r, \theta') d\theta'$ is the field-aligned coordinate, and $\hat{q}(r, \theta) = \frac{\mathbf{B} \cdot \nabla \zeta}{\mathbf{B} \cdot \nabla \theta}$.

The gyrokinetic ion/fluid electron hybrid model^{25,28} is employed in this work. The ions are described by the gyrokinetic equation and solved with the δf PIC method.^{29,30} The electrons are described by a fluid model consisting of the electron continuity equation, the Ohm's law, and an isothermal condition for the electron temperature perturbation.

The electron continuity equation is written as

$$\begin{aligned} \frac{\partial \delta n_e}{\partial t} + \mathbf{B} \cdot \nabla \frac{n_0 \delta u_{\parallel e}}{B} + \delta \mathbf{B}_\perp \cdot \nabla \frac{n_0 u_{\parallel e0}}{B} + \delta \mathbf{B}_\perp \cdot \nabla \frac{n_0 \delta u_{\parallel e}}{B} \\ + \mathbf{v}_E \cdot \nabla (n_0 + \delta n_e) + \frac{1}{m_e \Omega_e B^2} \mathbf{B} \times \nabla B \cdot \nabla (\delta p_{e\perp} + \delta p_{e\parallel}) \\ + \frac{2n_0}{B^3} \mathbf{B} \times \nabla B \cdot \nabla \phi = 0, \end{aligned} \quad (3)$$

with $u_{\parallel e0}$ the equilibrium electron parallel flow and $\delta u_{\parallel e}$ the perturbed electron parallel flow. The perturbed electron pressure is $\delta p_{e\perp} = \delta p_{e\parallel} = n_e \delta T_e + T_e \delta n_e$, δT_e , and δn_e are perturbed electron temperature and perturbed electron density, respectively. The $\nabla (\delta p_{e\perp} + \delta p_{e\parallel})$ term on the left-hand-side of Eq. (3), hereafter referred to as the toroidal pressure term, arises from the guiding-center magnetic drift in a low- β plasma,²⁴ and the last term from the compressibility of the $\mathbf{E} \times \mathbf{B}$ drift. Both terms are induced by the toroidal effect.

For $n = 1$, the third term on the left-hand-side of Eq. (3), i.e., the kink term can be expressed as

$$\begin{aligned} \delta \mathbf{B}_\perp \cdot \nabla \left(\frac{n_0 u_{\parallel e0}}{B} \right) = - \frac{\partial A_\parallel}{\partial x} \frac{\partial}{\partial \theta} \left(\frac{n_0 e u_{\parallel e0}}{B} \right) \mathbf{b} \cdot \nabla r \times \nabla \theta \\ + \frac{\partial A_\parallel}{\partial y} \left[- \frac{\partial y}{\partial r} \frac{\partial}{\partial \theta} \left(\frac{n_0 u_{\parallel e0}}{B} \right) \right. \\ \left. + \frac{r_0}{q_0} \hat{q} \frac{\partial}{\partial r} \left(\frac{n_0 u_{\parallel e0}}{B} \right) \right] \mathbf{b} \cdot \nabla r \times \nabla \theta \\ + \frac{\partial A_\parallel}{\partial z} \left[\frac{\partial}{\partial r} \left(\frac{n_0 u_{\parallel e0}}{B} \right) \right] \mathbf{b} \cdot \nabla x \times \nabla z. \end{aligned} \quad (4)$$

It is important to include the last term for the $n = 1$ mode. The parallel vector potential A_\parallel is evolved according to

$$\frac{\partial A_\parallel}{\partial t} = E_\parallel - \nabla_\parallel \phi. \quad (5)$$

In this paper, a simple Ohm's law is used,

$$E_\parallel = \eta j_\parallel, \quad (6)$$

with η the resistivity. $j_\parallel = \delta j_{\parallel i} - en_0 \delta u_{\parallel e}$ is the parallel perturbed current where $j_{\parallel i}$ is the parallel ion current calculated from the ion distribution function.

The electron parallel flow velocity $\delta u_{\parallel e}$ is obtained from the Ampère's equation,

$$en_0 \delta u_{\parallel e} = \delta j_{\parallel i} + \frac{1}{\beta_u} \nabla_\perp^2 A_\parallel, \quad (7)$$

and then used in the electron continuity equation, Eq. (3), to evolve δn_e .

The electrostatic potential is obtained from the vorticity equation

$$- \frac{n_0}{T} \frac{\partial \phi}{\partial t} [1 - \Gamma_0(b)] = \frac{\partial}{\partial t} (q_i \overline{\delta n_i} - e \delta n_e). \quad (8)$$

This equation is derived by taking the time derivative of the quasi-neutral equation

$$-qn_p = q_i \overline{\delta n_i} - e \delta n_e, \quad (9)$$

where $n_p = -\frac{qn_0}{T} \sum_{\mathbf{k}_\perp} e^{i\mathbf{k}_\perp \cdot \mathbf{x}} \phi_{\mathbf{k}} [1 - \Gamma_0(b)]$, with $b = \frac{k_\perp^2 v_{ti}^2}{\Omega_i^2} = -\frac{v_{ti}^2}{\Omega_i^2} \nabla_\perp^2$, Γ_0 being the Γ -function, $v_{ti} = \sqrt{T/m_i}$ being the ion thermal velocity, and $\Omega_i = qB/m_i$ being the cyclotron frequency. The rate of change of the ion charge density in Eq. (8) is given by the ion continuity equation, which is obtained by integrating the ion gyrokinetic equation for δf_i .

We now derive an energy-like equation for diagnostics purpose. Write the electron continuity equation as

$$\frac{\partial \delta n_e}{\partial t} + \nabla \cdot (n_0 \delta u_{\parallel e} \mathbf{b}) - \left(\frac{\partial \delta n_e}{\partial t} \right)_R = 0, \quad (10)$$

where all the terms on the left-hand-side of Eq. (3), except the first two terms, are lumped into $(\partial \delta n_e / \partial t)_R$. Similarly, the ion continuity equation is written as

$$q_i \frac{\partial \overline{\delta n_i}}{\partial t} + \nabla \cdot (\delta j_{\parallel i} \mathbf{b} + \delta \mathbf{j}_{\perp i}) - q_i \left(\frac{\partial \overline{\delta n_i}}{\partial t} \right)_R = 0, \quad (11)$$

where the ion current in the second term comes from integrals that involve δf_i , while $(\partial \overline{\delta n_i} / \partial t)_R$ comes from integrals that involve the equilibrium ion distribution. Now multiply the vorticity equation by ϕ and integrate over space, making use of Eqs. (5) and (7), to obtain

$$\begin{aligned} \frac{dE}{dt} = & - \int \delta j_{\parallel i} E_{\parallel} dx + \int \delta \mathbf{j}_{\perp i} \cdot \nabla \phi dx - \int e n_0 \delta u_{\parallel e} E_{\parallel} dx \\ & + q_i \int \phi \dot{n}_p dx + q_i \int \phi \left(\frac{\partial \overline{\delta n_i}}{\partial t} \right)_R dx - e \int \phi \left(\frac{\partial \delta n_e}{\partial t} \right)_R dx, \end{aligned} \quad (12)$$

where

$$E = \frac{1}{2\beta_u} \int (\delta B_{\perp})^2 dx, \quad (13)$$

is the energy stored in the perturbed magnetic field. The first two terms on the right-hand-side can be interpreted as the (negative) parallel and perpendicular Joule heating rate on the ions and will be calculated when the kinetic ion effect on the tearing mode is studied in Sec. III.

For low- n perturbations, the Padé approximation $\Gamma_0(b) \approx \frac{1}{b+1}$ can be applied to the vorticity equation (8) as

$$-\nabla_{\perp}^2 \frac{\partial \phi}{\partial t} = \frac{q}{m_0} \left(B^2 - \frac{mT}{q^2} \nabla_{\perp}^2 \right) \frac{\partial}{\partial t} (q_i \delta n_i - e \delta n_e), \quad (14)$$

the second term on the right-hand-side indicates the FLR effect.

The main closure relation for this fluid electron model is the linearized isothermal condition for the perturbed electron temperature,³¹

$$\mathbf{b} \cdot \nabla \delta T_e + \frac{\delta B_{\perp}}{B} \cdot \nabla T_e = 0. \quad (15)$$

This isothermal condition is derived from the electron drift kinetic equation by assuming $\omega \ll k_{\parallel} v_{Te}$, where ω is the characteristic frequency of the fluctuations, v_{Te} is the electron thermal speed, and k_{\parallel} is the parallel wave number.³¹

It can be seen that both the Ampère's equation (7) and the vorticity equation (14) have the form of the Laplacian equation

$$-\nabla_{\perp}^2 f = S. \quad (16)$$

The Laplacian operator can be expressed in the field-aligned coordinates as

$$\begin{aligned} \nabla_{\perp}^2 f = & \frac{\partial^2 f}{\partial x^2} |\nabla x|^2 + 2 \frac{\partial^2 f}{\partial x \partial y} \nabla x \cdot \nabla y + \frac{\partial^2 f}{\partial y^2} |\nabla y|^2 \\ & + \frac{\partial f}{\partial x} \nabla \cdot \nabla x + \frac{\partial f}{\partial y} \nabla \cdot \nabla y + \frac{\partial^2 f}{\partial x \partial z} \nabla x \cdot \nabla z + \frac{\partial^2 f}{\partial y \partial z} \nabla y \cdot \nabla z \\ & + \nabla \cdot \left(\frac{\partial f}{\partial z} \nabla z \right) - (\mathbf{b} \cdot \nabla)^2 f. \end{aligned} \quad (17)$$

In a field solver with a high- n approximation, only the first three terms are retained. However, this is not a good approximation for low- n perturbations. It is possible to expand the current solver to 3D by using a finite difference method to discretize the terms that involve z -derivative. This leads to a linear system with a much increased number of unknowns, difficult for a direct linear equation solver. We have attempted to move all the terms that involve z -derivative to the right-hand-side and use an iterative method to account for them, but the iterative scheme is found to diverge for the $n = 1$ mode. We therefore seek an alternative method that is based on the Laplacian operator expressed directly in the flux coordinate (r, θ_f, ζ) . Thus the Laplacian operator is expanded as

$$\begin{aligned} \nabla_{\perp}^2 f = & \frac{\partial^2 f}{\partial r^2} |\nabla r|^2 + \frac{\partial^2 f}{\partial \theta_f^2} |\nabla \theta_f|^2 + 2 \frac{\partial^2 f}{\partial r \partial \theta_f} \nabla r \cdot \nabla \theta_f \\ & + 2 \frac{\partial^2 f}{\partial r \partial \zeta} \nabla r \cdot \nabla \zeta + 2 \frac{\partial^2 f}{\partial \theta_f \partial \zeta} \nabla \theta_f \cdot \nabla \zeta + \frac{\partial^2 f}{\partial \zeta^2} |\nabla \zeta|^2 \\ & + \frac{\partial f}{\partial r} \nabla \cdot \nabla r + \frac{\partial f}{\partial \theta_f} \nabla \cdot \nabla \theta_f + \frac{\partial f}{\partial \zeta} \nabla \cdot \nabla \zeta - (\mathbf{b} \cdot \nabla)^2 f. \end{aligned} \quad (18)$$

The first two terms in the second line vanish because the ζ -direction is orthogonal to the (r, θ_f) -plane. The last term in the third line is found to be negligible, as expected for field-aligned perturbations. Note that the periodic boundary condition is applied in both θ_f and ζ . Equation (16) can be solved with a hybrid spectral method in the poloidal and toroidal angle, and a finite difference method in radius. For a given toroidal mode number n , f is decomposed as $f_n(r, \theta_f, \zeta) = \sum_m f_{nm}(r) \cdot e^{in\zeta + im\theta_f}$. The metric coefficients, such as $|\nabla r|^2$ and $|\nabla \theta_f|^2$, are decomposed as $g(r, \theta_f) = \sum_{m'} g_{m'}(r) \cdot e^{im'\theta_f}$. The right hand side S is represented as $S_n(r, \theta_f, \zeta) = \sum_{m_0} S_{nm_0}(r) \cdot e^{in\zeta + im_0\theta_f}$. The poloidal mode number m and m_0 satisfy $|m_{(0)} + nq(r)| < p$ to keep the toroidal coupling effect. The parameter p controls the range of k_{\parallel} included. Typically $p = 3$ is sufficient to ensure convergence in this paper.

With the spectral decomposition, Eq. (16) is now written as

$$\begin{aligned} - \sum_m \sum_{m'} \left\{ \left[|\nabla r|_{m'}^2 \frac{\partial^2 f_{nm}(r)}{\partial r^2} - m^2 |\nabla \theta_f|_{m'}^2 f_{nm}(r) - n^2 |\nabla \zeta|_{m'}^2 f_{nm}(r) \right. \right. \\ \left. \left. + 2im (\nabla r \cdot \nabla \theta_f)_{m'} \frac{\partial f_{nm}(r)}{\partial r} + (\nabla \cdot \nabla r)_{m'} \frac{\partial f_{nm}(r)}{\partial r} \right. \right. \\ \left. \left. + im (\nabla \cdot \nabla \theta_f)_{m'} f_{nm}(r) + \left(\frac{n+m}{q} \right)^2 |\nabla \zeta|_{m'}^2 f_{nm}(r) \right] \cdot e^{im\theta_f + im'\theta_f} \right\} \\ = \sum_{m_0} S_{nm_0}(r) \cdot e^{im_0\theta_f}. \end{aligned} \quad (19)$$

For every poloidal component m_0 , one can multiply both sides of this equation by $e^{-im_0\theta_f}$ and then integrate in θ_f on $[-\pi, \pi]$. Then Eq. (19) can be transformed into a set of coupled equations,

$$\begin{aligned}
 & - \sum_{m+m'=m_0} \left\{ \left[|\nabla r|_{m'}^2 \frac{\partial^2 f_{nm}(r)}{\partial r^2} - m^2 |\nabla \theta_f|_{m'}^2 f_{nm}(r) - n^2 |\nabla \zeta|_{m'}^2 f_{nm}(r) \right. \right. \\
 & + 2im(\nabla r \cdot \nabla \theta_f)_{m'} \frac{\partial f_{nm}(r)}{\partial r} + (\nabla \cdot \nabla r)_{m'} \frac{\partial f_{nm}(r)}{\partial r} \\
 & \left. \left. + im(\nabla \cdot \nabla \theta_f)_{m'} f_{nm}(r) + \left(\frac{n+m}{q} \right)^2 |\nabla \zeta|_{m'}^2 f_{nm}(r) \right\} = S_{nm_0}(r).
 \end{aligned} \tag{20}$$

The toroidal coupling effect is induced by $m' \neq 0$ components in the metric coefficients. For cylindrical geometry with $m' = 0$, there is no poloidal mode coupling.

Using a second order finite difference scheme for the radial derivatives, the final discretized equation is:

$$\begin{aligned}
 & - \sum_{m+m'=m_0} \left\{ \left[\frac{|\nabla r|_{m'}^2}{(\Delta r)^2} - \frac{2im(\nabla r \cdot \nabla \theta_f)_{m'} + (\nabla \cdot \nabla r)_{m'}}{2\Delta r} \right] \cdot f_{nm}(j-1) \right. \\
 & + \left[im(\nabla \cdot \nabla \theta_f)_{m'} - m^2 |\nabla \theta_f|_{m'}^2 - n^2 |\nabla \zeta|_{m'}^2 \right. \\
 & - 2 \frac{|\nabla r|_{m'}^2}{(\Delta r)^2} \left(\frac{n+m}{q} \right)^2 |\nabla \zeta|_{m'}^2 \cdot f_{nm}(j) \\
 & \left. \left. + \left[\frac{|\nabla r|_{m'}^2}{(\Delta r)^2} + \frac{2im(\nabla r \cdot \nabla \theta_f)_{m'} + (\nabla \cdot \nabla r)_{m'}}{2\Delta r} \right] \cdot f_{nm}(j+1) \right\} \right. \\
 & = S_{nm_0}(j).
 \end{aligned} \tag{21}$$

Here, $f_{nm}(j) = f_{nm}(x_j)$ with x_j the radial grid point. Equation (21) is applied to both Ampère’s equation, Eq. (7), and the vorticity equation, Eq. (14).

In deriving the discretized equation, Eq. (21), the Dirichlet boundary condition $f(r_{in}) = f(r_{out}) = 0$ is used, where r_{in} and r_{out} are the inner and outer radial boundaries. The particle weights of ions hitting the radial boundaries are also set to zero, and the ions are put back inside the simulation domain at the poloidal angle where their unperturbed trajectories would intersect the boundary surfaces again. The magnetic axis is excluded because the Jacobian for the field-aligned coordinates is singular at $r=0$. For the $m=0$ and $m=1$

components, the solution of the Laplace equation near $r=0$ is linear in radius, and the Dirichlet boundary is not appropriate, especially for the kink mode. We have implemented the linear boundary condition for $m=0$ and $m=1$ ³² and verified that the results in this paper are not changed.

Besides the exclusion of the magnetic axis from simulation, the present study of low- n modes has two other limitations. The first limitation comes from the field model. It is common to use the potentials (A_{\parallel}, ϕ) to represent the electromagnetic fields in the study of high- n drift-wave turbulence. However, for low- n modes the accuracy of this model remains to be verified with more complete field models. The second limitation is that the plasma equilibrium is not self-consistent. Simulations are performed to study certain parameter dependence, e.g., the dependence of the tearing mode growth rate on the aspect ratio or the ion temperature. For simplicity, the parameters are varied independently and arbitrarily, with no attempt to ensure consistency with the Grad–Shafranov equation.

We first use the method of “manufactured solution” to verify the low- n solver based on Eq. (21). An arbitrary analytical solution f_A is prescribed, and then the source term $S_A = -\nabla^2 f_A$ is calculated directly and assigned to the grids. The numerical solution f_N is then calculated from S_A with the new field solver and compared with the original f_A .

Here, we set $f_A = \sum_{m,n} \frac{1}{\sigma_{m,n}} \exp\left(-\frac{(x-\xi_{m,n})^2}{800\sigma_{m,n}^2}\right) \cos(m\theta_f + n\zeta)$, where $\sigma_{m,n} = 1 + \left| \frac{n-2m}{10n} \right|$, $\xi_{m,n} = \frac{lx}{2} + \frac{20(n-2m)}{n}$, $n = -1$, and $0 \leq m \leq 3$. $-2 \leq m' \leq 2$ is kept in numerical calculation. The comparison between the numerical solution and analytic solution is shown in Fig. 1(a). It can be seen that a good agreement can be achieved for all the poloidal components. For reference, the numerical solution without poloidal mode coupling is also shown in Fig. 1(b). It is obtained by setting $m' = 0$. Without the poloidal coupling effect, there is a large deviation between f_N and f_A for every (m, n) . This illustrates the importance of mode coupling effects in toroidal geometry.

Gyrokinetic codes often solve the Poisson equation and the parallel Ampère’s equation in the poloidal plane. In effect, the term in Eq. (18) that is proportional to $\nabla \zeta$, and the last term, are neglected. Neglecting the toroidal derivative is a poor approximation for low aspect-ratio tokamaks, $R/a \sim 1$. The low- n field solver developed here does not have this limitation. It can be combined with the usual high- n solvers in an integrated simulation of both micro-turbulence and low- n MHD modes such as the energetic particle-driven Alfvén waves.

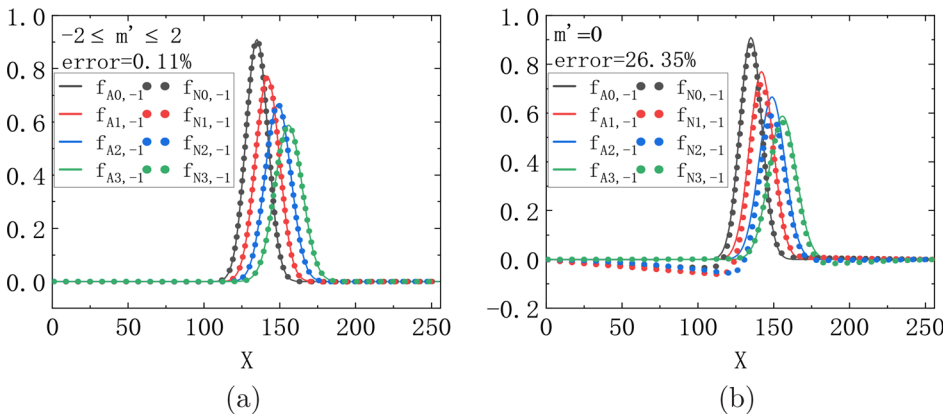


FIG. 1. Comparison between the numerical solution f_N and the analytic solution f_A for each poloidal harmonics (a) with toroidal coupling and (b) without toroidal coupling. The error is defined as $error = \sum_{m,n} \int \left| \frac{f_A - f_N}{f_N} \right| dx$.

In the following, we apply the low- n solver to the $n = 1$ resistive tearing mode in the toroidal geometry. This study extends the previous studies in cylindrical plasmas²⁶ as well as in toroidal plasmas.¹²

III. SIMULATION OF THE TOROIDAL RESISTIVE TEARING MODE

In the tokamak experiment, it is relatively easy to control the safety factor profile to avoid the most dangerous ($m = 1, n = 1$) tearing mode, which can couple with the $m > 1$ tearing modes strongly. However, other tearing modes such as the ($m = 2, n = 1$) mode and the ($m = 3, n = 2$) mode are usually unavoidable and can degrade the plasma confinement. In this section, we study the linear ($m = 2, n = 1$) resistive tearing mode, focusing on the effect of toroidicity and kinetic ions.

A concentric circles equilibrium ($R'_0 = 0, \kappa = 1, \text{ and } \delta = 0$) is used for simulations with parameters $B = 1.0 \text{ T}, R_0 = 1.0 \text{ m}$. The density profile is set to be constant as $n_{0i} = n_{0e} = 2.5 \times 10^{19} / \text{m}^3$. The temperature profiles are $T_e(r) = T_0(1 - r/a)^3$ and $T_i = \tau T_e$, with $T_0 = 0.1 \text{ keV}$. The plasma beta is $\beta = 4\mu_0 n_0 T_0 / B^2 = 0.002$. The resistivity η and the growth rate γ in the following are normalized to $\eta_0 = B / en_{0e} = 0.25 \Omega \text{ m}$ and $\omega_c = eB / m_i = 4.8 \times 10^7 \text{ Hz}$, respectively. The resistivities used in the following simulations range from $10^{-5} \Omega \text{ m}$ to $10^{-4} \Omega \text{ m}$ are much larger than the estimated collisional Spitzer resistivity $\sim \eta_s = 7 \times 10^{-7} \Omega \text{ m}$.³³ The inverse aspect ratio is defined as $\epsilon = a / R_0$. The safety factor profile is set as $q(r) = 1.62 - 2.59(r/a) + 5.50(r/a)^2$, which is plotted in Fig. 2.

A. Toroidal effect on the tearing mode

First, the effect of toroidal coupling on the tearing mode is examined by simulations. The ions are cold with $\tau = 10^{-3}$ to suppress any ion kinetic effects. Figure 3 shows the radial mode structures of the tearing mode for three dominant poloidal harmonics in cylindrical and toroidal geometry. In cylindrical geometry, there is no poloidal coupling, and poloidal harmonics in the fluctuation with $m \neq 2$ vanish. In the toroidal geometry, the $m = 1$ and $m = 3$ harmonics are generated through poloidal coupling, though their amplitudes are smaller than that of $m = 2$.

Next, we study the effect of the inverse aspect ratio on the radial structure of the tearing mode. Simulations with three different values

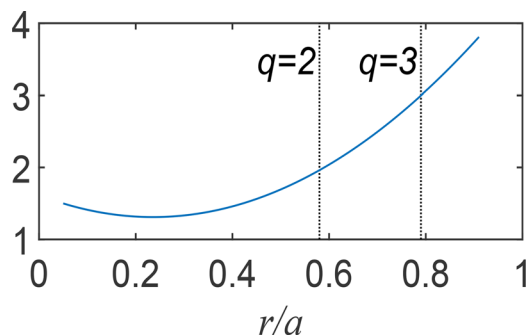


FIG. 2. Radial safety factor profile, where a is the minor radius. The dashed lines show the position of the $q = 2$ rational surface at $r/a = 0.58$ and the position of the $q = 3$ rational surface at $r/a = 0.79$.

of inverse aspect ratio (varying a), $\epsilon = 0.15, 0.25, \text{ and } 0.35$, are performed. The results are shown in Fig. 4. Figure 4(e) shows that the width of $\phi_{m=2}$ decreases with increasing ϵ ; the structure of $A_{\parallel m=2}$ remains unchanged which is shown in Fig. 4(b). The magnitudes of the subdominant components, $A_{\parallel m=1,3}$ and $\phi_{m=1,3}$, increase with ϵ . This indicates that the toroidal coupling effect is enhanced as ϵ increases, as is expected.

The mode structures of ϕ and A_{\parallel} on the poloidal cross section, for $\epsilon = 0.15$ and $\epsilon = 0.35$, are shown in Fig. 5. The in-out asymmetry of the mode structure appears due to the in-out asymmetry of the toroidal magnetic field line,¹² and this phenomenon becomes more prominent with ϵ increase.

The effects of the toroidicity on the tearing mode growth rate are investigated numerically by scanning the resistivity η for different values of ϵ . The simulation results are shown in Fig. 6(a). Toroidicity has a clear reduction effect on the growth of the tearing mode due to the favorable average curvature⁶ and the poloidal coupling effect. The stabilizing effect increases as ϵ increases. For $\epsilon = 0.35$ and $\eta = 5 \times 10^{-5}$, toroidicity can reduce the growth rate by about 50%. For sufficiently small resistivity, the tearing mode would be completely damped by Glasser effect.³⁴ However, when the tearing layer becomes very thin, more radial grid points are needed to ensure sufficient radial resolution. As an initial value simulation, the simulation needs to be very long to observe a clear growing eigenmode, or to conclude that the mode is stabilized. Because of this limitation, only large values of resistivity are considered. It also can be found that the theoretical scaling $\gamma \sim \eta^{3/5}$ ¹⁴ is generally satisfied except for the case with small ϵ and large η . This is because the theoretical scaling is obtained with the constant $-\psi$ assumption that is applicable only when the tearing layer is sufficiently narrow. As ϵ decreases and η increases, the tearing layer increases accordingly and eventually the constant $-\psi$ assumption breaks down.

The effects of toroidicity on the frequency of tearing modes are also briefly investigated numerically by scanning η for different ϵ , as shown in Fig. 6(b). The mode propagates in the electron diamagnetic direction, and the frequencies are at the level of the electron diamagnetic frequency, $\omega_{*e} = k_{\theta} \nabla T_e / eB$ (for a flat density profile). The magnitude of the mode frequency increases with increasing η and decreases with ϵ . When the ion temperature increases (Sec. III B), the magnitude of the frequency decreases. In general, the mode frequency is found to be much smaller than the growth rate and requires much longer simulation to have an accurate estimate. For this reason, we focus on the growth rate in the following investigations.

The dependence of the radial mode width on the resistivity is plotted in Fig. 7 for $\epsilon = 0.25$. Here, the radial mode width is defined by the full width at half maximum of the radial mode structure of ϕ . It can be observed that the toroidal effect can increase the radial mode width. Moreover, there is no clear scaling law between the radial mode width and η in this situation. We found that the broaden effect is mainly induced by the toroidal pressure term in the electron continuity equation (3). This can be seen in Fig. 7, when the toroidal pressure term is turned off in the simulation, the dependence of the radial mode width on the resistivity is consistent with the results in cylindrical geometry and meets the scaling of $\Delta \sim \eta^{2/5}$, which is consistent with the theoretic scaling of the current layer width Δ_c in Ref. 14. It also can be found that, neglecting the toroidal pressure term, the toroidal effect can weakly narrow the tearing mode.

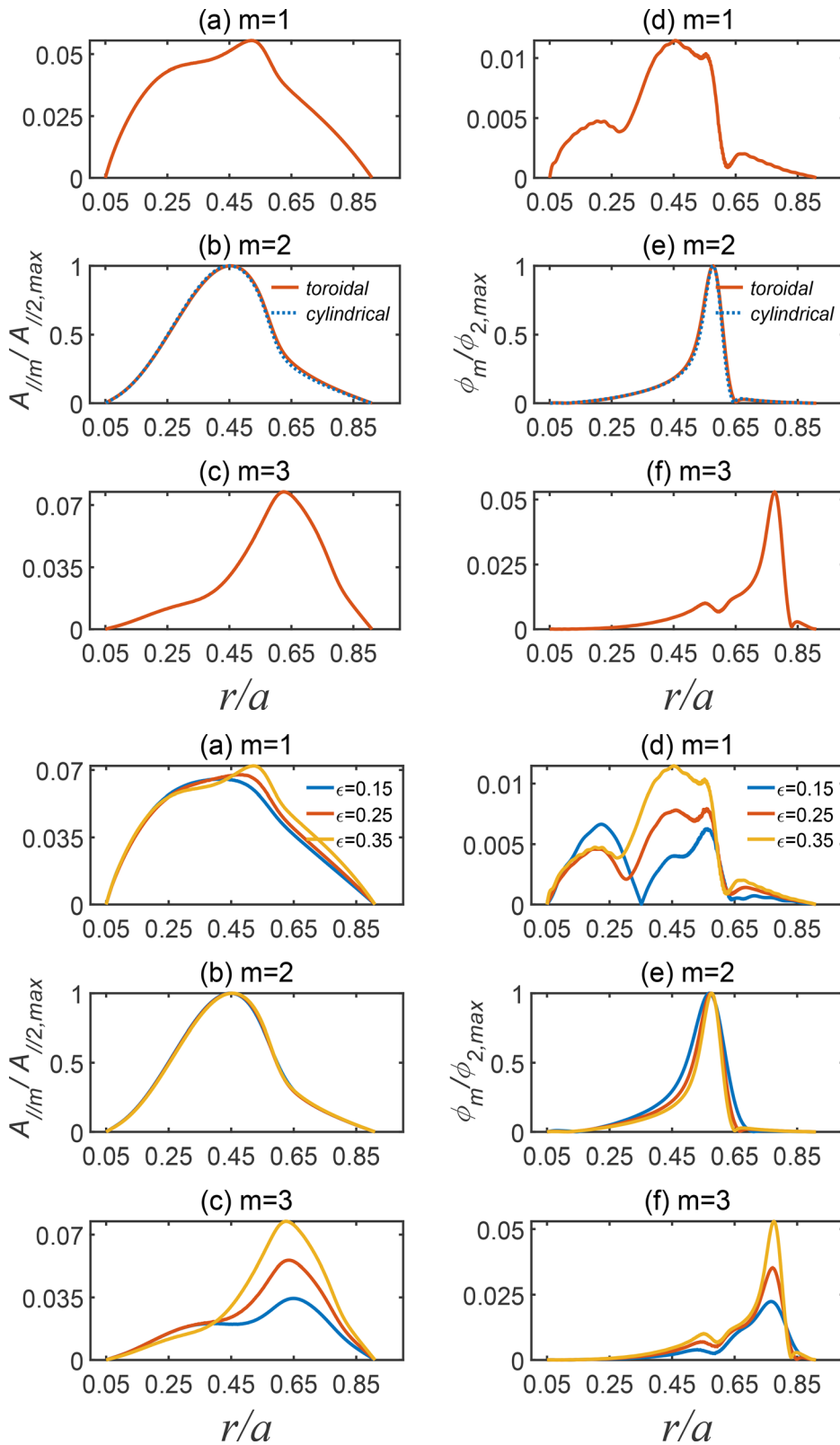


FIG. 3. The wave forms of $A_{||}$ [(a)–(c)] and ϕ [(d)–(f)] for $m=1, 2, 3$ components. The dashed lines in (b) and (e) show the waveforms in cylindrical geometry while the solid lines everywhere show the toroidal wave forms when $\epsilon = 0.35$ and $\eta = 2 \times 10^{-4}$. All the profiles are normalized to the maximum absolute values of $A_{||2}$ and ϕ_2 .

FIG. 4. The wave forms of $A_{||m}$ and ϕ_m for $\epsilon = 0.15, \epsilon = 0.25,$ and $\epsilon = 0.35$ with $\eta = 5 \times 10^{-4}$. All the profiles are normalized to the maximum absolute values of $A_{||2}$ and ϕ_2 .

31 August 2023 11:59:02

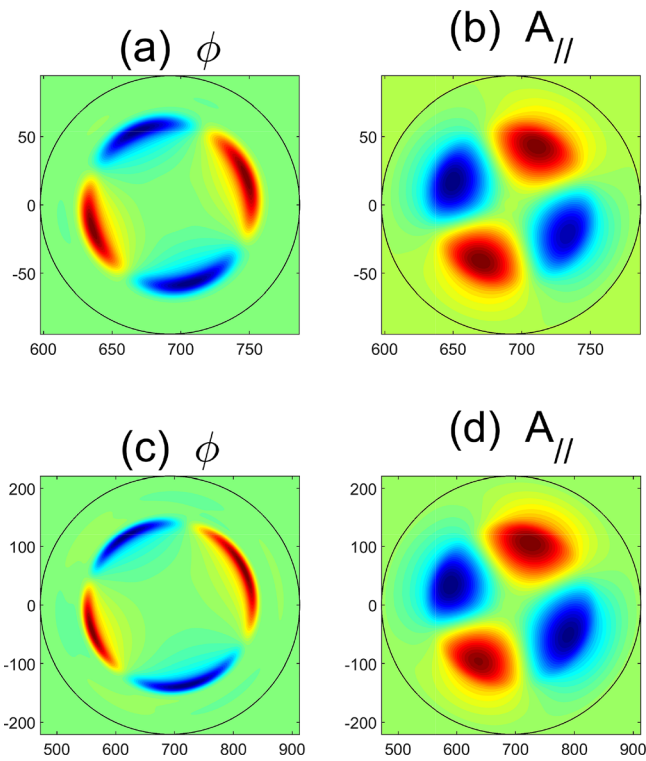


FIG. 5. Poloidal mode structures of ϕ (left) and A_{\parallel} (right) for $\epsilon = 0.15$ (up) and $\epsilon = 0.35$ (down).

B. Kinetic ion effects on the tearing mode

In this section, the kinetic ion effects on the tearing mode are studied by increasing the ion temperature to be the same as the electron temperature, $\tau = 1$. The inverse aspect ratio is $\epsilon = 0.25$.

First, the dependence of the growth rates of the tearing mode on η for cold ions ($\tau = 10^{-3}$) and thermal ions ($\tau = 1$) is compared in Fig. 8. It can be seen that the kinetic ions can decrease the growth rate of the tearing mode effectively, and the suppressing effect increases with η . This might be because more kinetic ions can interact with the tearing mode as the radial mode width grows with η . The simulation results still agree with the theoretic scaling in the small η limit.

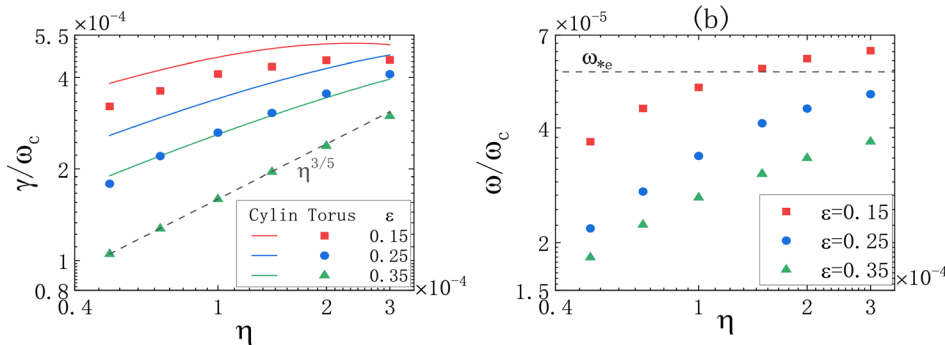


FIG. 6. (a) The dependence of growth rate on η for different ϵ in cylindrical and toroidal geometry. (b) The dependence of mode frequency on η for different ϵ in toroidal geometry. The dashed line is the electron diamagnetic frequency at the $q = 2$ surface for $\epsilon = 0.25$.

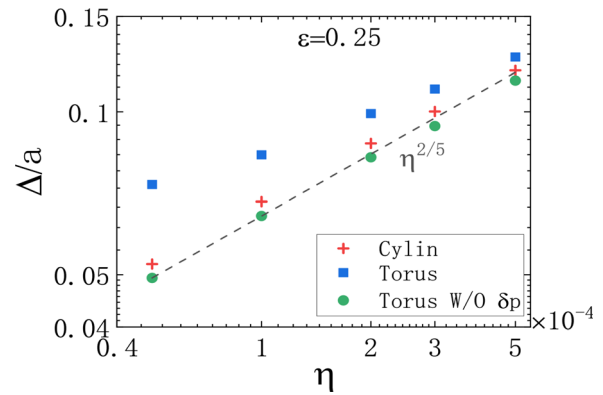


FIG. 7. The dependence of the radial mode width on η for $\epsilon = 0.25$. The radial mode width is defined by the full width at half maximum of the radial mode structure of ϕ .

It is known that the ion kinetic effect is closely related to the ion gyro-radius $\rho_i = m_i \sqrt{T_i} / qB$. Theory predicts that the classic growth rate of the collisional tearing mode follows $\gamma \sim \rho_i^{-2/5}$.¹⁴ Therefore, $\gamma \sim m_i^{-2/5}$ and $\gamma \sim T_i^{-1/5}$ can be easily derived. These two scaling can be verified through numerical simulation by parameter scan, which is shown in Fig. 9. It can be observed that the growth rate decreases as ion temperature and ion mass increase, and the growth rates agree with the theoretical prediction well.

A finite ion temperature introduces the FLR effect on the tearing mode that is present in cylindrical plasmas. The FLR effect is important only at low resistivity, and other kinetic ion effects are found to be not important in cylindrical geometry.²⁶ Toroidicity introduces particle trapping and radial magnetic drift to the guiding-center motion. We first perform numerical experiments to test the FLR effect and the effect of magnetic drift (v_D) in the ion guiding-center motion. The results are shown in Table I. The FLR effect is turned off (FLR = 0) by replacing the gyro-averaged value of a quantity with the value at the guiding-center location. The magnetic drift is turned off ($v_D = 0$) by removing the magnetic drift from the guiding-center motion.

As listed in Table I, the simulation results with/without the FLR and/or magnetic drift effect of thermal ions are compared to that with the cold ions. By comparing case 1 with case 2, we found that the results in the cold ions limit can be recovered by turning off the FLR and the v_D effects in the simulations with thermal ions. By comparing

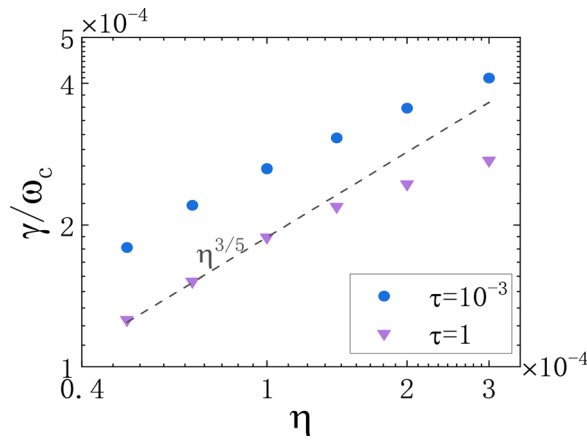


FIG. 8. The growth rates of the tearing mode for different η for $\tau = 10^{-6}$ and $\tau = 1$.

case 2 with case 3, the FLR effect is shown to be unimportant, which is consistent with the result in cylindrical geometry.²⁶ By comparing case 3 with case 4, the growth rate of the tearing mode decreases significantly by including the magnetic drift. This suggests that kinetic ions affect the tearing mode mainly through the magnetic drift.

To gain further insight into the kinetic ion effect, a joule heating diagnostics for the ions is performed. That is, the ion joule heating terms in Eq. (12) are calculated and divided by two times the magnetic energy, $2E$ (the field energy grows at twice the linear growth rate, hence the factor of 2), giving a value of growth rate which can be interpreted as the contribution of the term to the mode growth rate. The contributions from trapped and passing ions are calculated separately. Other terms on the right-hand-side of Eq. (12) are also examined, and it is found that the main instability drive comes from the last term, as it contains the kink term that drives the tearing mode. Damping comes from the first four terms which stand for the ion parallel joule heating, the ion perpendicular joule heating, the electron parallel joule

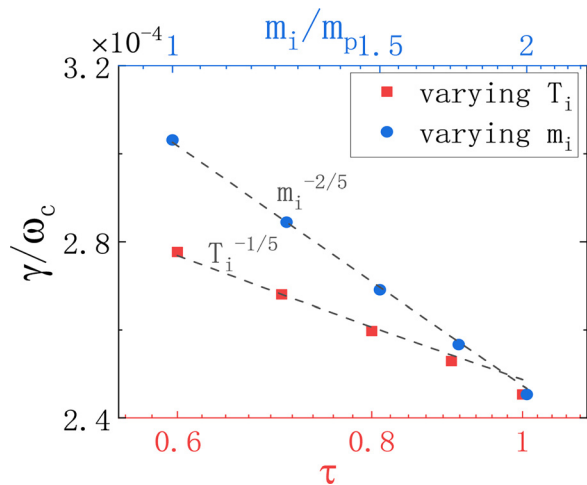


FIG. 9. The growth rates of the tearing mode for different T_i and m_i with $\eta = 2 \times 10^{-4}$.

TABLE I. FLR effect and magnetic drift effect on the tearing mode growth rates. The growth rates are normalized to the value from the cases with cold ions ($\tau = 0.001$).

	$\eta = 1 \times 10^{-4}$	$\eta = 2 \times 10^{-4}$	$\eta = 3 \times 10^{-4}$
1. $\tau = 10^{-3}$, FLR = 1, $v_D = 1$	1.00	1.00	1.00
2. $\tau = 1$, FLR = 0, $v_D = 0$	0.9954	0.9974	0.9964
3. $\tau = 1$, FLR = 1, $v_D = 0$	0.9981	0.9983	0.9969
4. $\tau = 1$, FLR = 1, $v_D = 1$	0.7146	0.6981	0.7015

heating and the energy spent on polarizing the ions, respectively. The ion term proportional to $(\frac{\partial \delta n_i}{\partial t})_R$ is found to be negligible. Notice that the term in the ion continuity equation that arises from the compressibility of the $E \times B$ motion is nearly canceled by the corresponding electron term, and only the residual due to the ion FLR effect is retained in the vorticity equation.²⁵ Thus ion effects mainly come from the two ion joule heating terms. As shown in Table II, the passing ions dominate over the trapped ions in both the parallel and perpendicular joule heating, and the parallel joule heating dominates over the perpendicular joule heating. The perpendicular joule heating vanishes for $\tau = 10^{-3}$, while it is substantial for $\tau = 1$. This is consistent with the previous test results on the effect of magnetic drift. Note however that the change in the total contribution to the growth rate from the ion joule heating is not equal to the change in the net linear growth rate. These observations suggest a complex role of kinetic ions.

The mode structure is also changed by the ion temperature, as is shown in Fig. 10. Changes in the mode structure are apparent for the $m = 1$ and $m = 3$ components, visible for the $m = 2$ component of the electric potential. Such changes in the mode structure will induce changes in the electron response as well, making it difficult to identify a single factor as an explanation of the observed kinetic ion effects in toroidal plasmas.

C. Plasma shaping effect on the tearing mode

Plasma shaping can strongly affect tokamak plasma confinement.³⁵⁻³⁷ Here, we briefly report the effect of shaping on the tearing mode. Simulations scanning the three parameters in the Miller model,²⁷ the Shafranov shift R_0' , the elongation κ , and the triangularity δ , are performed, and the results are shown in Fig. 11. It can be seen

TABLE II. The Joule heating rate of passing and trapped ions for $\tau = 10^{-3}$ and $\tau = 1$ when $\eta = 3 \times 10^{-4}$ and $\epsilon = 0.25$. The superscript "T" and "P" represent trapped and passing ions, respectively.

	$\tau = 10^{-3}$	$\tau = 1$
$\gamma(\text{mode})$	3.879×10^{-4}	2.650×10^{-4}
$\gamma(E_{\parallel} j_{\parallel i p})$	-3.209×10^{-4}	-3.874×10^{-4}
$\gamma(E_{\parallel} j_{\parallel i t})$	-1.624×10^{-5}	-1.919×10^{-5}
$\gamma(E_{\perp} j_{\perp i p})$	0	-7.163×10^{-5}
$\gamma(E_{\perp} j_{\perp i t})$	0	-1.388×10^{-5}

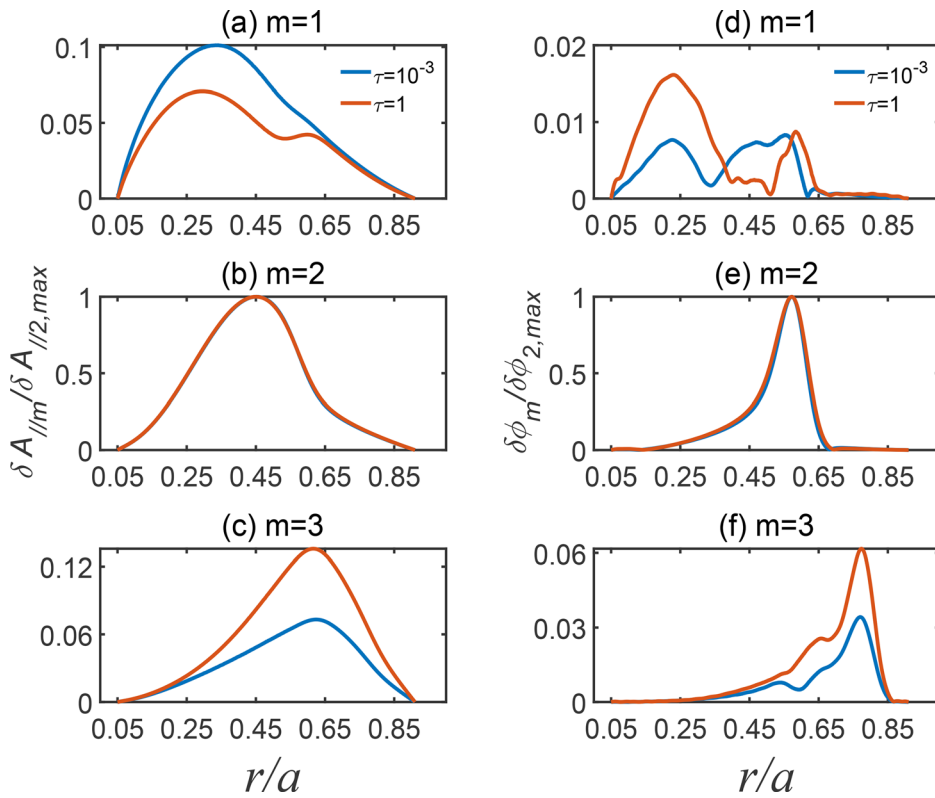


FIG. 10. The wave forms of $A_{\parallel m}$ and ϕ_m for $\tau = 0.001$ and $\tau = 1$. All the profiles are normalized to the maximum absolute values of $A_{\parallel 2}$ and ϕ_2 .

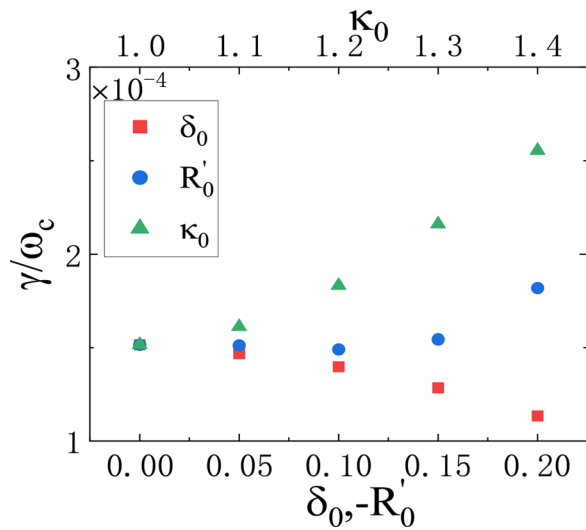


FIG. 11. The dependence of the growth rate on Shafranov shift R'_0 , elongation κ and triangularity δ for $\tau = 1$, $\epsilon = 0.25$, and $\eta = 7 \times 10^{-5}$.

that elongation has a significant destabilizing effect on the tearing mode, while triangularity has a significant stabilizing effect. The dependence of the growth rate on the Shafranov shift R'_0 is not monotonic. The mode structures of ϕ and A_{\parallel} for $R'_0 = -0.15$, $\kappa_0 = 1.3$,

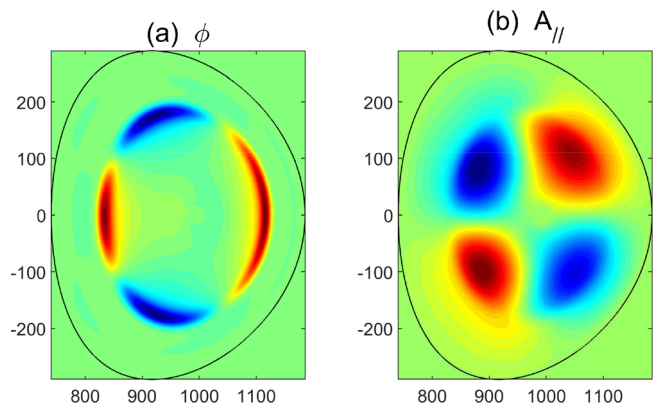


FIG. 12. The mode structures of (a) ϕ and (b) A_{\parallel} on the poloidal cross section for $R'_0 = -0.15$, $\kappa_0 = 1.3$, and $\delta_0 = 0.25$.

and $\delta_0 = 0.25$ are shown in Fig. 12. Although shaping in general has a significant effect on the tearing mode growth rate, we have verified that the conclusions drawn in Secs. III A and III B are not changed by shaping.

IV. CONCLUSION

A low- n field solver has been developed to extend GEM to the simulation of low- n MHD modes in toroidal geometry. The Padé approximation is used to cast the quasi-neutrality condition into the

form of a Laplacian equation. The fully 3D Laplacian operator is used instead of the common 2D Laplacian in the poloidal plane. The electric potential is expanded in both the toroidal direction and the poloidal direction. This spectral method reduces the number of unknowns, because for low- n modes, the number of significant poloidal harmonics is much smaller than the number of poloidal grids typically used in discretizing the 2D Laplacian.

The effects of toroidicity and kinetic ions on the resistive tearing mode are systematically studied and compared with analytic theory. The growth rate and the width of the tearing mode can be reduced by the toroidal effects. The toroidal pressure term in the electron continuity equation is found to increase the mode width. As the ion temperature increases, the growth rate of the tearing mode is significantly reduced.

In the future, the low- n field solver will be combined with the existing high- n solvers to study the interaction between low- n MHD waves, such as the energetic particles driven toroidal Alfvén eigenmodes and micro-turbulence. At present, such a simulation uses the high- n solvers for all toroidal numbers, therefore limited to $n \geq 3$. The new solver allows the inclusion of the $n=1$ TAE, for instance. We also plan to extend the simulation domain to include the magnetic axis and simulate the $n=1$ kink mode. The low- n solver can be readily extended to the axis by adopting the appropriate boundary condition. What remains is to populate the $r=0$ region with particles. A new algorithm for advancing the particles near the magnetic axis will be needed, as the existing algorithm, which advances particles in the field-line-following coordinates, is not applicable near $r=0$.

ACKNOWLEDGMENTS

We gratefully acknowledge Dr. Xiaoqing Yang for helpful discussion. This work was supported by the National MCF Energy R&D Program of China under Grant No. 2019YFE03060000, the National Key R&D Program of China under Grant No. 2017YFE0300406, and the National Natural Science Foundation of China under Grant Nos. 11975272 and 11905257. Y. Chen is supported by the SciDAC Center Advanced Tokamak Modeling Environment (AToM), Contract No. DE-SC0017992. The numerical calculations in this paper were performed on the ShenMa High Performance Computing Cluster in Institute of Plasma Physics, Chinese Academy of Sciences, and resources of the National Energy Research Scientific Computing Center (NERSC), which are supported by the Office of Science of the U.S. Department of Energy under Contract No. DE-AC02-05CH11231.

AUTHOR DECLARATIONS

Conflict of Interest

The authors declared that they have no conflicts of interest to this work.

DATA AVAILABILITY

The data that support the findings of this study are available from the corresponding author upon reasonable request.

REFERENCES

- ¹D. Biskamp, *Astrophys. Space Sci.* **242**, 165–207 (1996).
- ²R. a Treumann and W. Baumjohann, *Astron. Astrophys. Rev.* **23**, 4 (2015).
- ³M. Yamada, J. Yoo, J. Jara-Almonte, H. Ji, R. M. Kulsrud, and C. E. Myers, *Nat. Commun.* **5**, 4474 (2014).
- ⁴F. Schuller, *Plasma Phys. Controlled Fusion* **37**, A135 (1995).
- ⁵H. Furth, J. Killeen, and M. N. Rosenbluth, *Phys. Fluids* **6**, 459–484 (1963).
- ⁶H. Furth, P. Rutherford, and H. Selberg, *Phys. Fluids* **16**, 1054–1063 (1973).
- ⁷J. Drake, T. Antonsen, Jr., A. Hassam, and N. Gladd, *Phys. Fluids* **26**, 2509–2528 (1983).
- ⁸R. Hastie, F. Militello, and F. Porcelli, *Phys. Rev. Lett.* **95**, 065001 (2005).
- ⁹W. Zhang, Z. Ma, and S. Wang, *Phys. Plasmas* **24**, 102510 (2017).
- ¹⁰Y. Liu, A. Kirk, and E. Nardon, *Phys. Plasmas* **17**, 122502 (2010).
- ¹¹R. Izzo, D. Monticello, W. Park, J. Manickam, H. Strauss, R. Grimm, and K. McGuire, *Phys. Fluids* **26**, 2240–2246 (1983).
- ¹²D. Liu, W. Zhang, J. McClenaghan, J. Wang, and Z. Lin, *Phys. Plasmas* **21**, 122520 (2014).
- ¹³R. Hazeltine, D. Dobrott, and T. Wang, *Phys. Fluids* **18**, 1778–1786 (1975).
- ¹⁴J. Drake and Y. Lee, *Phys. Fluids* **20**, 1341–1353 (1977).
- ¹⁵H. Cai and G. Fu, *Phys. Plasmas* **19**, 072506 (2012).
- ¹⁶B. Rogers, S. Kobayashi, P. Ricci, W. Dorland, J. Drake, and T. Tatsuno, *Phys. Plasmas* **14**, 092110 (2007).
- ¹⁷H. Cai, S. Wang, Y. Xu, J. Cao, and D. Li, *Phys. Rev. Lett.* **106**, 075002 (2011).
- ¹⁸Y. Liu, R. Hastie, and T. Hender, *Phys. Plasmas* **19**, 092510 (2012).
- ¹⁹W. Hornsby, P. Miglano, R. Buchholz, L. Kroenert, A. Weikl, A. Peeters, D. Zarzoso, E. Poli, and F. Casson, *Phys. Plasmas* **22**, 022118 (2015).
- ²⁰D. R. Sydora, *Phys. Plasmas* **8**, 1929–1934 (2001).
- ²¹W. Wan, Y. Chen, and S. Parker, *Phys. Plasmas* **12**, 012311 (2005).
- ²²H. Doerk, F. Jenko, M. Pueschel, and D. Hatch, *Phys. Rev. Lett.* **106**, 155003 (2011).
- ²³Y. Lin, X. Wang, L. Chen, X. Lu, and W. Kong, *Plasma Phys. Controlled Fusion* **53**, 054013 (2011).
- ²⁴Y. Chen and S. Parker, *J. Comput. Phys.* **189**, 463–475 (2003).
- ²⁵Y. Chen, T. Munsat, S. E. Parker, W. W. Heidbrink, M. A. Van Zeeland, B. J. Tobias, and C. W. Domier, *Phys. Plasmas* **20**, 012109 (2013).
- ²⁶Y. Chen, J. Chowdhury, S. Parker, and W. Wan, *Phys. Plasmas* **22**, 042111 (2015).
- ²⁷R. Miller, M. S. Chu, J. Greene, Y. Lin-Liu, and R. Waltz, *Phys. Plasmas* **5**, 973–978 (1998).
- ²⁸Y. Chen and S. Parker, *Phys. Plasmas* **8**, 441–446 (2001).
- ²⁹S. Parker and W. Lee, *Phys. Fluids B* **5**, 77–86 (1993).
- ³⁰Y. Chen and S. Parker, *J. Comput. Phys.* **220**, 839–855 (2007).
- ³¹P. Snyder and G. Hammett, *Phys. Plasmas* **8**, 3199–3216 (2001).
- ³²J. McClenaghan, Z. Lin, I. Holod, W. Deng, and Z. Wang, *Phys. Plasmas* **21**, 122519 (2014).
- ³³L. Spitzer, *Physics of Fully Ionized Gases* (Courier Corporation, 2006).
- ³⁴A. Glasser, J. Greene, and J. Johnson, *Phys. Fluids* **18**, 875–888 (1975).
- ³⁵Y. Xiao and P. J. Catto, *Phys. Plasmas* **13**, 082307 (2006).
- ³⁶Z. Gao, P. Wang, and H. Sanuki, *Phys. Plasmas* **15**, 074502 (2008).
- ³⁷Z. Gao, *Phys. Plasmas* **17**, 092503 (2010).